Darcy?Forchheimer Radiative Flow of Micropoler CNT Nanofluid in Rotating Frame with Convective Heat Generation/Consumption

Authors:

Ebraheem O. Alzahrani, Zahir Shah, Wajdi Alghamdi, Malik Zaka Ullah

Date Submitted: 2019-12-03

Keywords: numerical techniques, electrochemical super-capacitors, HAM, micro-polar nanofluid, rotating system, porous media, heat source/sink, SWCNTs and MWCNTs, Darcy–Forchheimer relation

Abstract:

Since 1991, from the beginning of the carbon nanotube era, this has been a focus point for investigation due to its synthetic and simple nature. Unique properties like good stiffness, high surface area, and resilience of carbon nanotubes (CNTs) have been investigated in many engineering applications such as hydrogen storage, composite material, energy storage, electrochemical super-capacitors, transistors, sensors, and field-emitting devices. Keeping in view these applications, we investigate single and multi-walled CNTs nanofluid flow having water as the base fluid between parallel and horizontal rotating plates with microstructure and inertial properties. The thermal radiation effect is considered for variable phenomenon of heat generation/consumption. The principal equations are first symmetrically transformed to a system of nonlinear coupled ordinary differential equations (ODEs), and then, Homotopy Analysis Technique (HAM) and numerical method are employed for solving these coupled equations. The obtained analytical and numerical results are explained graphically and through different tables. The HAM and numerical results show an excellent agreement. The Skin friction and the Nusselt number are numerically calculated and then analyzed with the already published results, and these results are found to be in agreement with one another. The impact of important parameters are shown graphically.

Record Type: Published Article

Submitted To: LAPSE (Living Archive for Process Systems Engineering)

Citation (overall record, always the latest version):	LAPSE:2019.1255
Citation (this specific file, latest version):	LAPSE:2019.1255-1
Citation (this specific file, this version):	LAPSE:2019.1255-1v1

DOI of Published Version: https://doi.org/10.3390/pr7100666

processes

MDPI

Article

Darcy–Forchheimer Radiative Flow of Micropoler CNT Nanofluid in Rotating Frame with Convective Heat Generation/Consumption

Ebraheem O. Alzahrani [1], Zahir Shah [2,3,*], Wajdi Alghamdi [4] and Malik Zaka Ullah [1]

1 Department of Mathematics, Faculty of Science, King Abdulaziz University, P.O. Box 80203, Jeddah 21589, Saudi Arabia; eoalzahrani@kau.edu.sa (E.O.A.); zmalek@kau.edu.sa (M.Z.U.)
2 Center of Excellence in Theoretical and Computational Science (TaCS-CoE), SCL 802 Fixed Point Laboratory, Science Laboratory Building, King Mongkut's University of Technology Thonburi (KMUTT), 126 Pracha-Uthit Road, Bang Mod, Thrung Khru, Bangkok 10140, Thailand
3 Department of Mathematics, Abdul Wali Khan University, Mardan 23200, Pakistan
4 Department of Information Technology, Faculty of Computing and Information Technology, King Abdulaziz University, P.O. Box 80221, Jeddah 21589, Saudi Arabia; wmalghamdi@kau.edu.sa
* Correspondence: zahir.sha@kmutt.ac.th; Tel.: +66-988-813-762

Received: 2 September 2019; Accepted: 25 September 2019; Published: 27 September 2019

Abstract: Since 1991, from the beginning of the carbon nanotube era, this has been a focus point for investigation due to its synthetic and simple nature. Unique properties like good stiffness, high surface area, and resilience of carbon nanotubes (CNTs) have been investigated in many engineering applications such as hydrogen storage, composite material, energy storage, electrochemical super-capacitors, transistors, sensors, and field-emitting devices. Keeping in view these applications, we investigate single and multi-walled CNTs nanofluid flow having water as the base fluid between parallel and horizontal rotating plates with microstructure and inertial properties. The thermal radiation effect is considered for variable phenomenon of heat generation/consumption. The principal equations are first symmetrically transformed to a system of nonlinear coupled ordinary differential equations (ODEs), and then, Homotopy Analysis Technique (HAM) and numerical method are employed for solving these coupled equations. The obtained analytical and numerical results are explained graphically and through different tables. The HAM and numerical results show an excellent agreement. The Skin friction and the Nusselt number are numerically calculated and then analyzed with the already published results, and these results are found to be in agreement with one another. The impact of important parameters are shown graphically.

Keywords: Darcy–Forchheimer relation; SWCNTs and MWCNTs; heat source/sink; porous media; micro-polar nanofluid; rotating system; electrochemical super-capacitors; HAM; numerical techniques

1. Introduction

The novel progress in nanotechnology has produced a pioneering and inventive kind of heat-carrying liquid called nanoliquids, which are formed by the dispersal of tiny solid particles (1 nm–100 nm) in classical liquids. There are different kinds of classical liquids like bio-fluid, polymeric mixture, numerous oils, lubricants, water, toluene, refrigerants, ethylene glycol, etc. which can carry heat through very short ranges and are broadly used for various engineering and technological purposes. In order to improve the heat transport rate of such liquids, the nanoparticles of different materials are scattered consistently in these classical fluids. Carbon nanotubes (CNTs) are nanomaterials with diameters below 100 nm. CNTs can be refined or produced to retain definite properties such as optical transmissions, electrical conductivity, and gas absorption. CNTs were

introduced by Iijima [1]. Different CNTs studies based on structure, usage, characteristics, and shapes can be found in Ciraci et al. [2], Novoselov et al. [3] and Casari et al. [4]. CNTs have significant applications in nanotechnology, sensor devices, storage of gas, air refinement devices, conductive plastics, hard water, and many more. Due to such real-world applications, the investigators have shown great devotion to the field of nanotechnology [5–7]. CNTs based on nanoliquid flow over extending sheets has been studied by Imtiaz et al. [8]. Different features of CNTs in chemical reactions and in melting during Darcy–Forchheimer flow has been investigated by Hayat [9]. Mahanthesh and others [10] have inspected the magneto hydro dynamic (MHD) flow of CNT nanofluids by taking into consideration the impact of thermal energy. MHD slip flow with CNTs and convective heat energy transfer has been presented by Raja et al. [11]. Shah et al. [12] has analyzed the Darcy–Forchheimer radiative flow of CNTs in a circulating frame. Jawad et al. [13] examined the nonlinear thermal impact on the three-dimensional CNT flow with viscous dissipation. Sheikholeslami et al. [14–16] have numerically treated the nanofluid flow in porous media by considering different channels. Shah et al. [17–19] has studied the nanofluid flow by considering the impacts of Brownian motion, thermophoresis, and Hall current between parallel plates. The effects of radiations and heat source/sink on the flow of a nanofluid over a stretching surface has been given by Dawar et al. [20]. A more brief survey on the analysis of stretching surface can be found with different fluid models in Shah et al. [21] and Ameen et al. [22]. The Casson fluid flow with radiation impacts in rotating channels has been examined by Dawar et al. [23]. Sohail et al. [24] has analyzed Ferrofluid flow during the impact of magnet and drug targeting. This fluid is also discussed on the stretching surface by Zeeshan et al. [25]. Further analysis of Ferrofluid with different physical explorations can be found in Majeed et al. [26].

Eringon [27] has given for the first time the clue of micro-polar fluid, and then it was briefly explained by Lukaszewicz [28]. Mohammeadein and Gorla [29] have undertaken the MHD micro-polar fluid flow over a stretching surface. The Darcy–Forchheimer micro-polar nanofluid flow in a rotating frame which results in heat generation/absorption has examined by Khan et al. [30]. Many industrial as well as environmental systems, for example, geo-thermal energy and heat exchanger operating systems, contain the convective heat transfer flow on porous media. For investigation of all the relevant characteristics, Forchheimer [31] has explained the additional relation in momentum. Muskat [32] has called this additional relation the Forchheimer relation. The initial study on Darcian free convention flow has performed by Cheng et al. [33]. Later on, the appropriate similarity alternation has been suggested by Merkin [34]. The general form of the Merkin research was deliberated by Nakayama et al. [35]. The MHD flow of Darcy–Forchheimer nanofluid has been deliberated by Jawad et al. [36]. Further relevant studies can be found in Shah et al. [37], Khan et al. [38], Nasir et al. [39], Islam et al. [40] and Ellahi et al. [41]. Raju et al. [42] has determined the MHD flow of nanofluids over a cone. The uniform magnetic force effect on the thermal behavior of the water-based nanofluid has been explained by Sheikholeslami et al. [43]. Rehman et al. [44] has undertaken the MHD-flow of carbon micro-polar nanofluids in a rotating frame by taking into account the convective heat transfer during the flow. Some interesting studies related to nanofluid non-Newtonian flow field can be found in Hayat et al. [45], Tian et al. [46], Hsiao and Long [47] and Hsiao and Long [48]. The entropy production analysis during the carbon nanotube flows in a rotatory system by considering together the Hall and Ion-slip effects has been given by Feroz et al. [49]. A more brief survey on the entropy generation with different geometrical and analytical explorations can be found in Ellahi et al. [50,51]. Additional information about the relevant study can be explored in Sheikholeslami et al. [43], Ellahi et al. [52], Rehman et al. [44], Feroz et al. [49], Khan et al. [53] and Shah et al. [54].

In the current paper, single and multi-walled (CNT) nanofluid flow by taking water as the base fluid between parallel and horizontal rotating plates with microstructures and inertial properties is studied. Influences of nonlinear heat generation/absorption are presented. The important key factors are described in the output. Homotopy Analysis Technique (HAM) and the NDsolve [55–60] technique are used for solution purposes. In Section 2 the problem and geometry is explained. The results

obtained are discussed in Section 3. The tables are presented and discussed in Section 4. This work is concluded in Section 5. Homotypic operators and theory are used in the solution section.

2. Problem Statement

Consider the steady flow of micro-polar nanofluid water-based carbon nanotubes among parallel plates. The geometry of the model is chosen such that both the nanofluid and plates are circulating around the y-axis with angular speed $\bar{\omega}$, as shown in Figure 1. The separation distance between the two plates is h. Equal and opposite forces are acting on the lower plate along x-axis which can stretch it with linear velocity $u = \alpha x$, where $\alpha > 0$. A Darcy–Forchheimer model is assumed for the porosity. The temperature and concentration at the lower plates are taken as $T = T_h$ and $C = C_h$, respectively. Thermal radiation is assumed for irregular suction/injection. After applying these assumptions, the governing equations can be written as follows [9,10,18,19]:

$$u_x + v_y + w_z = 0, \tag{1}$$

$$uu_x + vu_y + 2w\bar{\omega} = -\frac{P_x}{\rho_f} + \left(\nu_{nf} + \frac{\beta}{\rho_f}\right)(u_{xx} + u_{yy}) + \frac{\beta}{\rho_f}N_y - \frac{1}{\rho_f}\left(\frac{\nu_{nf}}{B}\right)u - \frac{1}{\rho_f}Eu^2, \tag{2}$$

$$uv_x + vv_y = -\frac{P_y}{\rho_f} + \left(v_{xx} + v_{yy}\right) + \frac{\beta}{\rho_f}N_x, \tag{3}$$

$$uw_x + vw_y - 2u\bar{\omega} = \left(\nu_{nf} + \frac{\beta}{\rho_f}\right)(w_{xx} + w_{yy}) - \frac{1}{\rho_f}\left(\frac{\nu_{nf}}{B}\right)w - \frac{1}{\rho_f}Ew^2, \tag{4}$$

$$uT_x + vT_y + wT_z = \alpha^*\left(T_{xx} + T_{yy} + T_{zz}\right) + \frac{1}{(\rho c)_p}\left(q''' - q_y^{rd}\right), \tag{5}$$

$$uN_x + vN_y = -\frac{\gamma}{\rho_j}\left(N_{xx} + N_{yy}\right) - \frac{2\beta N}{\rho_j} + \frac{\beta}{\rho_j}\left(v_x - u_y\right). \tag{6}$$

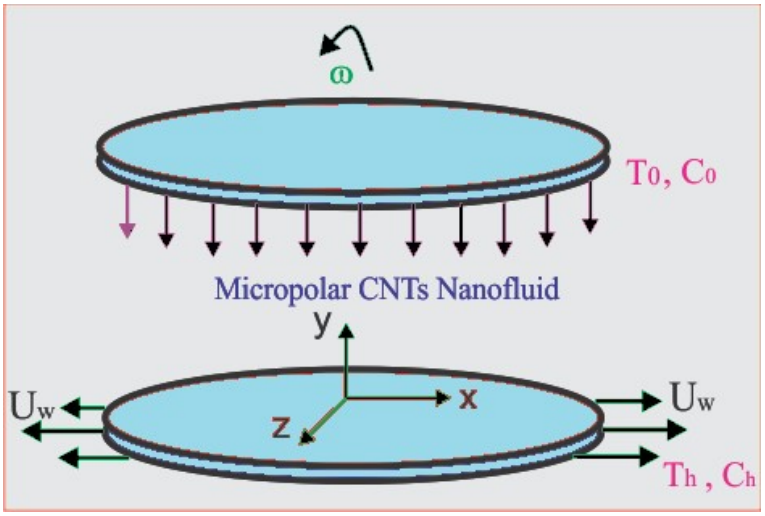

Figure 1. Geometrical sketch of the phenomenon.

In the above equations, ν_{nf}, μ, ρ_f, N, $\bar{\omega}$, β, B, $E = C_b(bx)^{-1/2}$, C_b, T, α^*, D_B, D_T, c_p, τ^*, and C represent kinematic viscosity, dynamic viscosity, density, micro rotational velocity, angular velocity, vertex viscosity, magnetic field strength, variable inertia coefficient, drag coefficient, temperature, thermal diffusivity, Brownian diffusion coefficient, thermophoretic diffusion coefficient, specific heat, fraction between nanofluid and heat capacity, and concentration of nanoparticles,

respectively. The thermal radiation is mathematically defined as $q^{rd} = -\frac{16\Theta^*}{3k^*}\frac{\partial T^4}{\partial y}$. After Taylor series expansion [12,18], we get

$$\frac{\partial q^{rd}}{\partial y} = -\frac{16T_0^3\Theta^*}{3k^*}\frac{\partial T^2}{\partial^2 y}. \tag{7}$$

The term q''' in Equation (5) is used for the irregular heat generation/consumption and is given as follows:

$$q''' = \frac{\beta u}{xv}\left(I(T-T_h)f'(\xi) + (T-T_h)J\right), \tag{8}$$

where I represents the temperature coefficient and J represents the space dependence of heat sink and source. The necessary boundary restriction are given by

$$\begin{aligned} u = \alpha x, v = w = 0, T = T_h, N = -\frac{\partial u}{\partial y}k \quad \text{at} \quad y = 0, \\ u = v = w = 0, T = T_0, N = \frac{\partial u}{\partial y}k \quad \text{at} \quad y = h. \end{aligned} \tag{9}$$

For the CNT nanofluids, the following model is presented by Xue [61].

$$\begin{aligned} \mu_{nf} = \frac{\mu_f}{(1-\varphi)^{2.5}}, \nu_{nf} = \frac{\mu_{nf}}{\rho_{nf}}, \alpha_{nf} = \frac{\mu_n f}{(\rho c_p)_{nf}}, \rho_{nf} = (1-\varphi)\rho_f + \varphi\rho_{CNT}, \\ (\rho c_p)_{nf} = (\rho c_p)_f\left((1-\varphi) + \left(\frac{(\rho c_p)_{CNT}}{(\rho c_p)_f}\right)\varphi\right), \\ \frac{k_{nf}}{k_f} = \frac{1-\varphi+2\varphi\left(\frac{k_{CNT}}{k_{CNT}-k_f}\right)ln\left(\frac{k_{CNT}+k_f}{2k_f}\right)}{1-\varphi+2\varphi\left(\frac{k_f}{k_{CNT}-k_f}\right)ln\left(\frac{k_{CNT}+k_f}{2k_f}\right)}. \end{aligned} \tag{10}$$

Introducing the new transformation [18,19], we get

$$\begin{aligned} u = \alpha x f'(\xi),\ v = -\alpha h f(\xi),\ N = -\frac{\alpha x G(\xi)}{h}, \\ w = \alpha x g(\xi),\ \theta(\xi) = \frac{T-T_h}{T_0-T_h},\ \xi = \frac{y}{h}\ . \end{aligned} \tag{11}$$

Using Equation (10) in Equations (2)–(9), we get

$$\xi_1\left(\left(\frac{1}{\xi_2}+P_1\right)f^{iv} + P_1G'' - \gamma f' - 2E_r f' f''\right) - Re(f' f'' - f f''') - 2N_r g' = 0, \tag{12}$$

$$\xi_1\left(\left(\frac{1}{\xi_2}+P_1\right)g'' - \gamma g - E_r g^2\right) + Re(fg' - gf') + 2N_r f' = 0, \tag{13}$$

$$\frac{1}{\xi_1}\left(\xi_3 + \frac{4}{3}Rd\right)\theta'' - (I_1 f' + J_1\theta) = 0, \tag{14}$$

$$\xi_1\left(P_2G'' - P_1(2G + f'')\right) - P_3Re(Gf' - G'f) = 0. \tag{15}$$

We have used the following symbols for simplification:

$$\xi_1 = \left((1-\varphi) + \left(\frac{(\rho c_p)_{CNT}}{(\rho c_p)_f}\right)\varphi\right),\ \xi_2 = (1-\varphi)^{2.5},\ \xi_3 = \frac{k_{nf}}{k_f} \tag{16}$$

$$\begin{aligned} f = g = 0, \quad f^{'} = \theta = \varphi = 1, \quad G = -kf^{''}, \quad \text{at} \quad \xi = 0, \\ f^{'} = g = \theta = \varphi = 0, \quad f = \delta = 0, \quad G = kf^{''}, \quad \text{at} \quad \xi = 1. \end{aligned} \tag{17}$$

In the above equations, the different parameters are defined as Rotation parameter ($N_r = \frac{2\bar{\omega}h^2}{\nu_{nf}}$), permeability ($\gamma = \frac{h^2\nu_{nf}}{aB}$), coefficient of inertia ($E_r = \frac{h^2 C_b B^{-0.5}}{\rho}$), coupling ($P_1 = \frac{\beta}{\mu}$), transpiration parameter ($\delta = \frac{v_0}{h}$), viscosity gradient ($P_2 = \frac{\nu_s}{\nu_{nf}h^2}$), Reynold number ($Re = \frac{ah^2}{\nu_{nf}}$), micro-polar fluid constant ($P_3 = \frac{j}{h^2}$), volume friction of nanofluid (φ), thermal conductivity (k), and thermal radiation ($Rd = \frac{4T_0^3\eta}{(\rho c_p)_f \beta K}$). Here, I_1 and J_1 signify temperature- and space-dependent coefficients heat generation and absorption, where at $I_1 > 0$ and $J_1 > 0$, they link to inner heat source and, at $I_1 < 0$ and $J_1 < 0$, they correspond to inner heat sink. The skin friction (C_f) and Nusselt number (Nu) are defined as follows:

$$C_f = \xi_1\left(\frac{1}{\xi_2} + P_1\right)f^{''}(0) + P_1 G(0), Nu = -\left(\xi_3 + \frac{4}{3}Rd\right)\theta^{'}(0). \tag{18}$$

3. Results and Discussion

This section is devoted to studying graphically the effects produced by different physical variables on profiles of velocity components ($f^{'}(\xi)$, $g(\xi)$, $G(\xi)$) and temperature ($\theta(\xi)$) for single-walled carbon nanotubes (SWCNTs) and multi-walled carbon nanotubes (MWCNTs). These parameters are nanoparticle volume fraction φ, permeability parameter γ, rotation parameter N_r, Reynolds number Re, inertial coefficient E_r , thermal radiation parameter Rd, coupling P_1 , temperature-dependent coefficient J_1, and space-dependent parameter I_1.

The dependence of $f^{'}(\xi)$ as well as $g(\xi)$ on φ is shown in Figure 2. From Figure 2a, it is clear that, with the escalating φ, $f^{'}(\xi)$ shows an increasing behavior in the domain $0.0 \leq \xi < 0.5$, whereas it displays a reducing trend in the zone $0.5 < \xi \leq 1.0$. It is further evident that the increasing (decreasing) trend for SWCNTs is more rapid as compared to MWCNTs. Figure 2b shows that $g(\xi)$ varies inversely with respect to ξ up to about $\xi = 0.4$ and, beyond this value, shows an increase at fixed φ. By increasing the value of φ, $g(\xi)$ increases for both types of CNTs. Furthermore, the rate of variation of $g(\xi)$ is larger for MWCNTs as compared to SWCNTs. The effect of γ on $f^{'}(\xi)$ as well as $g(\xi)$ is depicted in Figure 2c,d, respectively. It is noted that $f^{'}(\xi)$ displays dual behavior with the increasing γ . The profile of $f^{'}(\xi)$ escalates in the zone $0 \leq \xi \leq 0.5$, whereas it declines beyond it, that is, in the range $0.5 < \xi \leq 1$, with the higher γ for both kinds of CNTs. From Figure 2d, it is clear that $g(\xi)$ enhances as we increase φ to larger values for both kinds of CNTs.

The dependence of the functions $f^{'}(\xi)$ as well as $g(\xi)$ on Re is depicted in Figure 3a,b. We observe from Figure 3a,c that $f^{'}(\xi)$ shows the same dual behaviour as in the case of Figure 2a,c. The function $f^{'}(\xi)$ increases in the range $0 \leq \xi \leq 0.5$, whereas it reduces in the range $0.5 \leq \xi \leq 1.0$ with larger Re. It is apparent from Figure 3b that $g(\xi)$ shows an increasing and measurable behaviour with respect to larger Re only for intermediate values of ξ. The dependence of $f^{'}(\xi)$ and $g(\xi)$ on E_r is depicted in the Figure 3c,d, respectively. The angular form of Newton's 2nd law indicates that the moment of inertia of a rotating system, which is the ratio of the net torque and angular acceleration, is a constant of motion. The higher values of inertial coefficient causes the fluid velocity to decline. The dual behavior is observed in both figures with the escalation in the inertial coefficient. This dual trend is a result of the frame rotation.

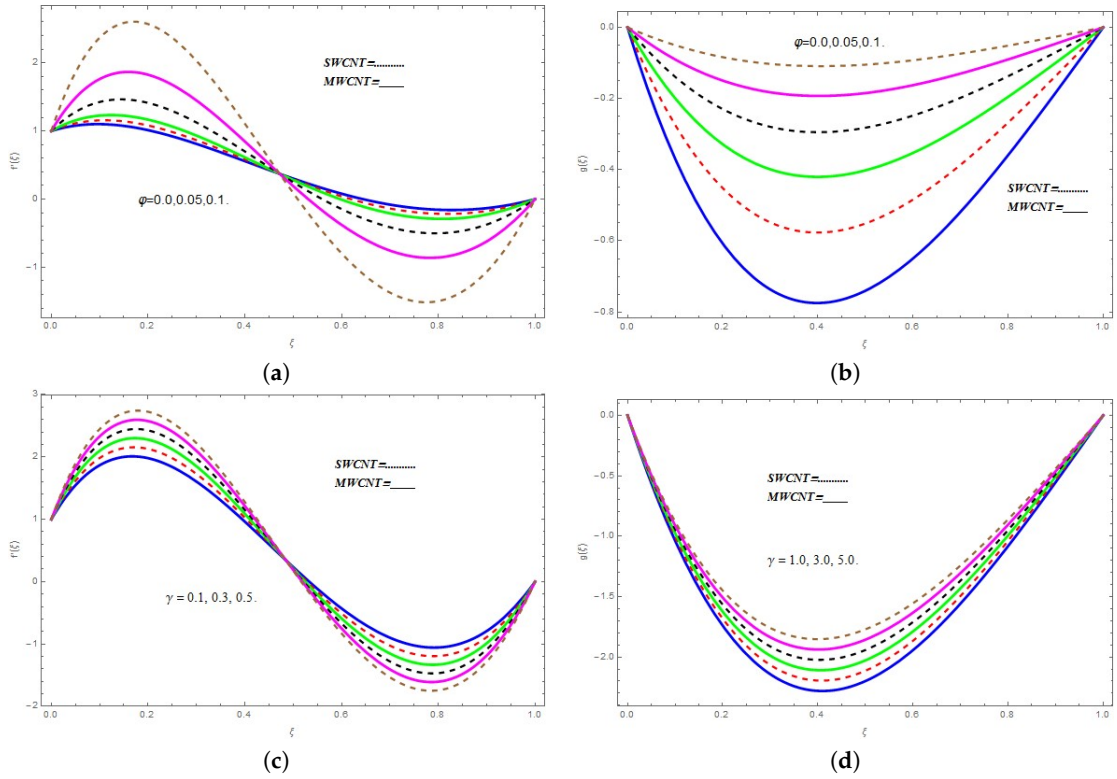

Figure 2. (**a**) Variation in $f^{'}(\xi)$ with different values of φ; (**b**) Variation in $g(\xi)$ with different values of φ; (**c**) Impact of γ on $f^{'}(\xi)$; (**d**) Impact of γ on $g(\xi)$

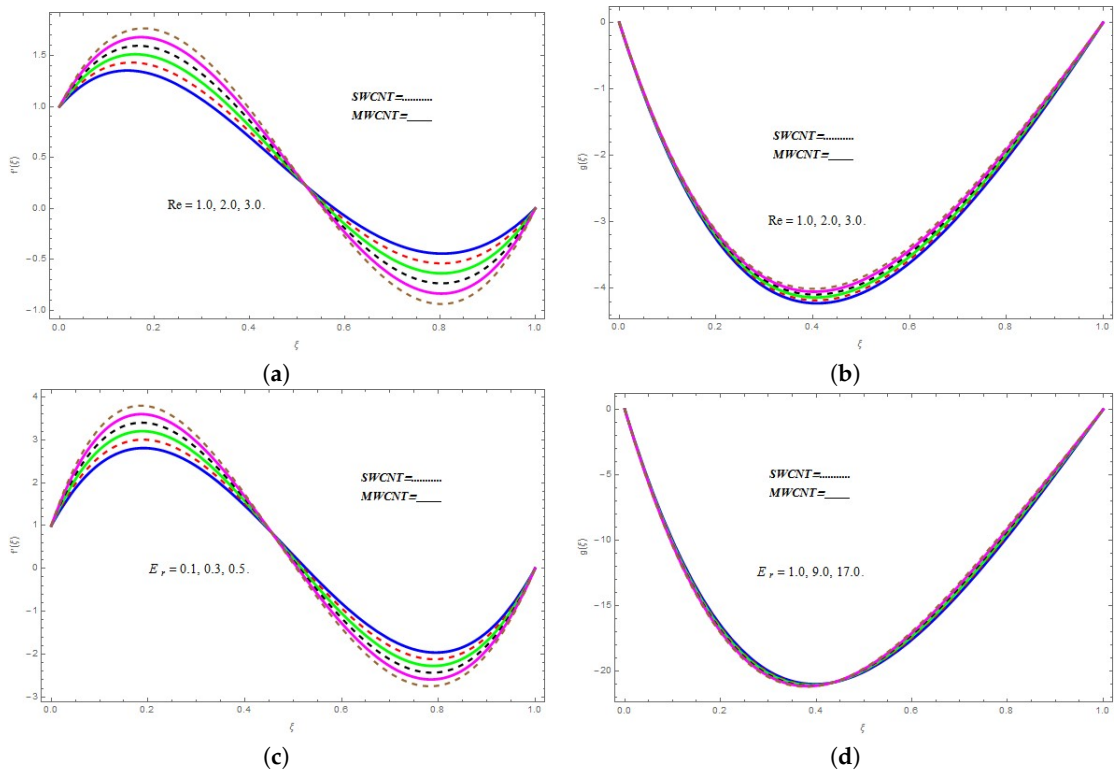

Figure 3. (**a**) Impact of Re on $f^{'}(\xi)$; (**b**) Impact of Re on $g(\xi)$; (**c**) Impact of E_r on $f^{'}(\xi)$; (**d**) Impact of E_r on $g(\xi)$

The influence of N_r on both $f^{'}(\xi)$ as well as $g(\xi)$ is displayed by Figure 4a,b. Within the restricted region, the escalating values of N_r first result in a decrease and, after that, cause a growing behavior

in the profile of $f^{'}(\xi)$. In the $0 \leq \xi \leq 0.6$ region, the increasing N_r displays a declining impact of $f^{'}(\xi)$ whereas, in the range $0.6 \leq \xi \leq 1.0$, shows a rising impact of $f^{'}(\xi)$, as shown in Figure 4a. The decreasing impact of $g(\xi)$ with the increasing values N_r is evident from Figure 4b for both kinds of CNTs. Figure 4c,d demonstrates the effect produced by P_1 on profiles of both $f^{'}(\xi)$ as well as $g(\xi)$. The coupling parameter defines the strength of the applied force in an interaction. It determines the strength of the interaction part with respect to the kinetic part. The escalating P_1 shows a dual behavior in the $f^{'}(\xi)$ profile. $f^{'}(\xi)$ increases in the domain $0 \leq \xi \leq 0.55$, while it reduces in the zone $0.55 \leq \xi \leq 1.0$ for SWCNTs as well as for MWCNTs. The rate of variation is faster for SWCNTs in comparison with MWCNTs. The dependence of $g(\xi)$ on P_1 is plotted in Figure 4d. This graph again depicts that $g(\xi)$ changes at a faster rate with increasing P_1 for SWCNTs.

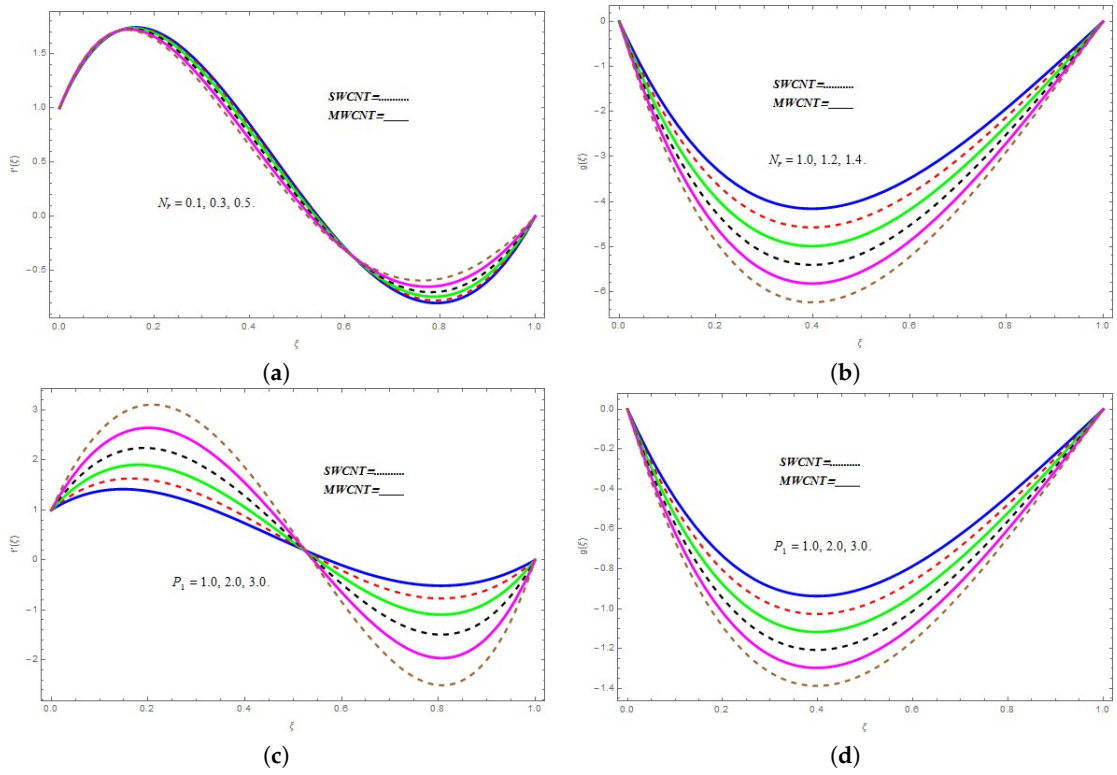

Figure 4. (**a**) Impact of N_r on $f^{'}(\xi)$; (**b**) Impact of N_r on $g(\xi)$; (**c**) Impact of P_1 on $f^{'}(\xi)$; (**d**) Impact of P_1 on $g^{(}\xi)$

The influence of φ on $\theta(\xi)$ is displayed in the Figure 5a. The rising values of φ shows an increasing trend in the $\theta(\xi)$ profile up to $\xi = 0.8$, and then, the different curves start to overlap for both types of CNTs. The effect of Rd on $\theta(\xi)$ is plotted in Figure 5b. The thermal radiations have a useful role in the heat energy transformation during the fluid flow process. The increasing thermal radiation values enhance the boundary layer flow rate, which results in the fluid temperature rising. Therefore, the temperature function $\theta(\xi)$ profile enhances for the higher values of Rd. Figure 5c,d depicts the influence of J_1 and I_1 on the temperature function $\theta(\xi)$. Both figures display the increasing effect of J_1 and I_1 on $\theta(\xi)$.

The effect of φ on velocity function $G(\xi)$ is plotted in Figure 6a. The higher values of φ escalates the velocity function $G(\xi)$. Similar impacts of P_1 and Re on velocity function $G(\xi)$ can be seen in Figure 6b,c, respectively.

The comparison between HAM results and numerical computations for the velocity and temperature profiles are displayed in Figure 7a–d. We see that the results obtained from analytical calculations and numerical computations are in excellent agreement for the undertaken study.

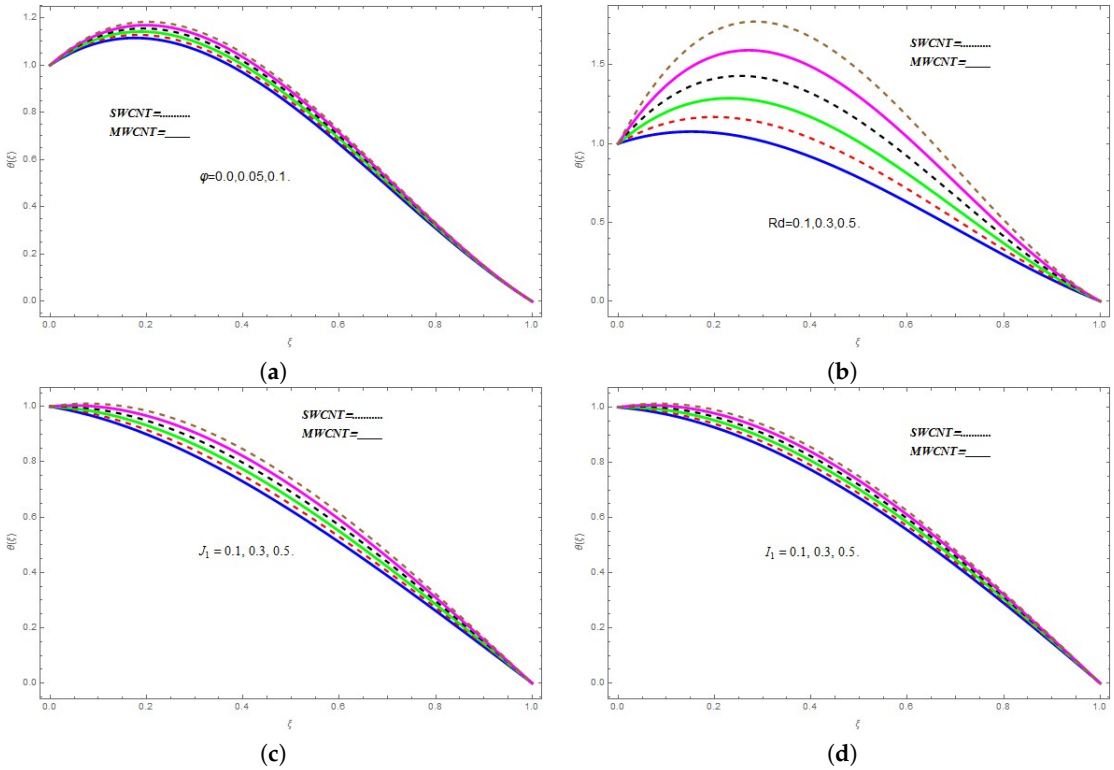

Figure 5. (**a**) Variations in $\theta(\xi)$ under different values of φ; (**b**) Impact of Rd on $\theta(\xi)$; (**c**)Impact of J_1 on $\theta(\xi)$; (**d**) Impact of I_1 on $\theta(\xi)$

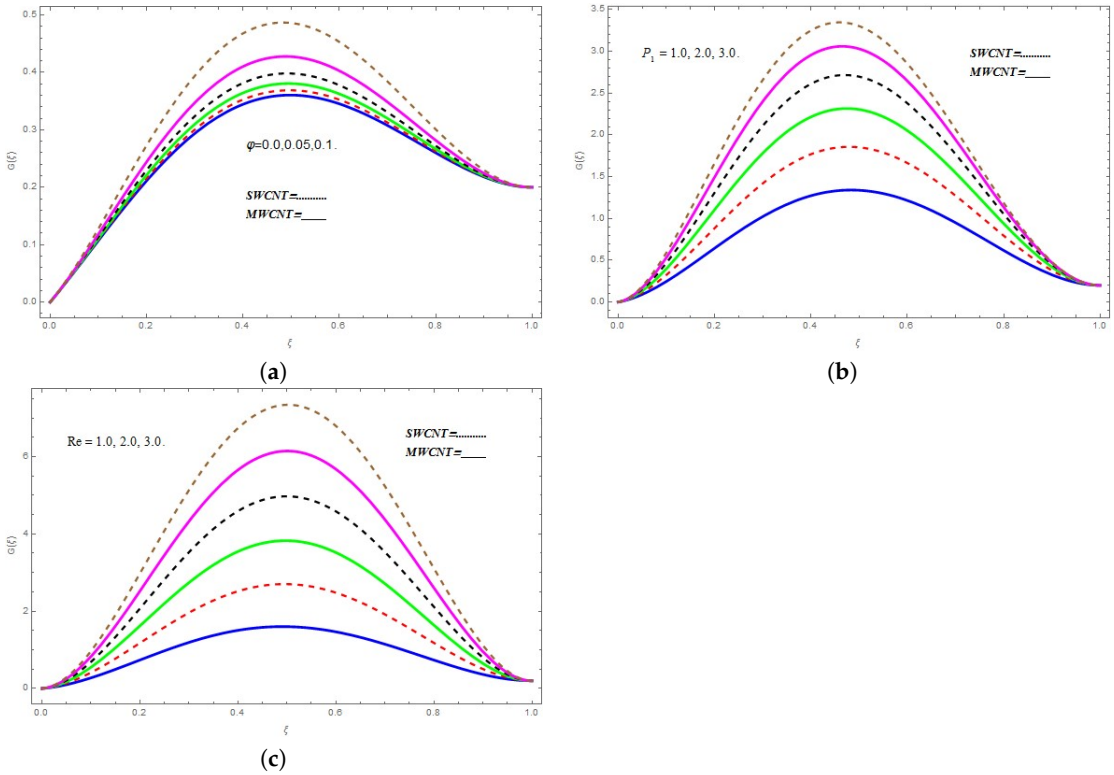

Figure 6. (**a**) Impact of φ on $G(\xi)$; (**b**) Variations in $G(\xi)$ under different values of P_1; (**c**) Impact of Re on $G(\xi)$

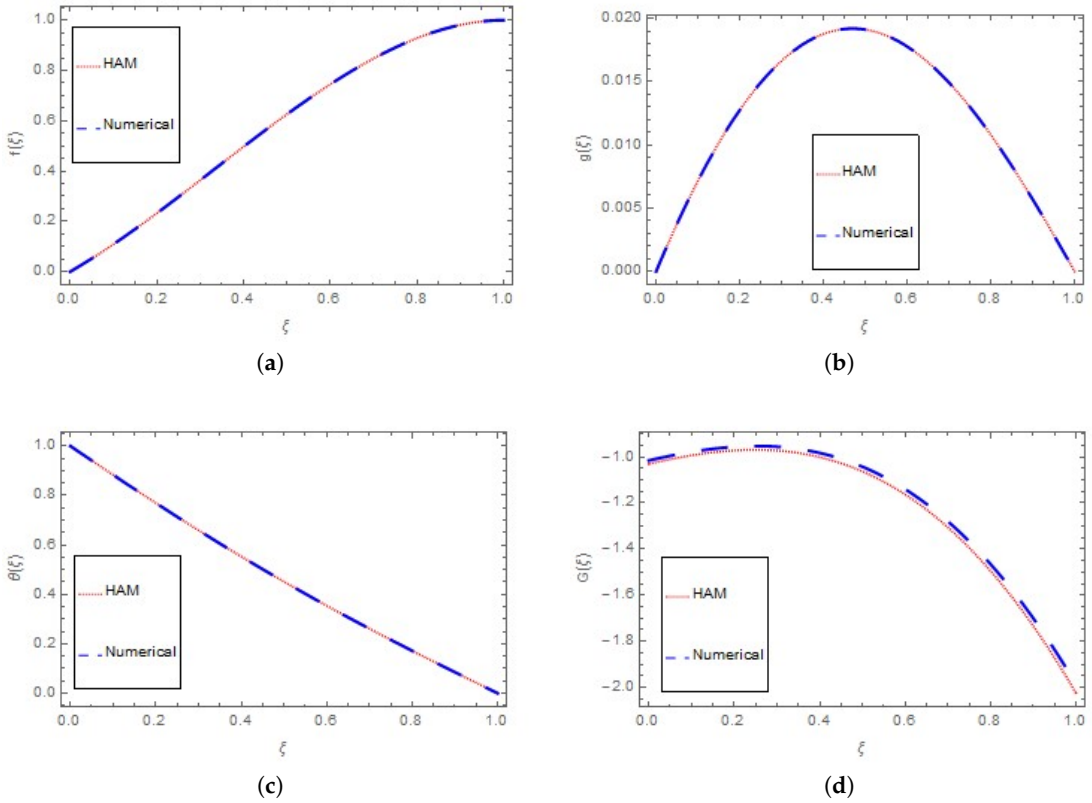

Figure 7. (**a**) Homotopy Analysis Method and Numerical method comparasion for $f(\xi)$; (**b**) Homotopy Analysis Method and Numerical method comparasion for $g(\xi)$; (**c**) Homotopy Analysis Method and Numerical method comparasion for $\theta(\xi)$; (**d**) Homotopy Analysis Method and Numerical method comparasion for $G(\xi)$

4. Tables Discussion

The comparison between analytical and numerical results for velocities, temperature, and concentration profiles is given in Tables 1–4. From these tables, an excellent agreement between HAM and the numerical technique (ND-Solve Techniques) can be seen. The impact of physical quantities like C_{fx} , C_{fy}, and Nu_x for SWCNTs as well as for MWCNTs is shown in Tables 5 and 6. The results obtained in the present study are then compared to the already published results [56]. It is found that both the present and published results are in agreement with each other.

Table 1. Comparision of HAM and Numerical results for $f(\xi)$.

ξ	HAM	Numerical Solution	Absolute Error
0.0	0.000000	0.000000	0.000000
0.2	0.232368	0.232374	6.268670×10^{-6}
0.4	0.496777	0.496789	0.000012
0.6	0.744737	0.744747	0.000010
0.8	0.928319	0.928323	3.595600×10^{-6}
1.0	1.000000	1.000000	6.712830×10^{-6}

Table 2. Comparision of HAM and Numerical results for $f(\xi)$.

ξ	HAM	Numerical Solution	Absolute Error
0.0	0.000000	0.000000	0.000000
0.2	0.012272	0.012272	1.023590×10^{-7}
0.4	0.018772	0.018772	1.820060×10^{-8}
0.6	0.017780	0.017780	1.174780×10^{-7}
0.8	0.010785	0.010785	1.308180×10^{-7}
1.0	$-4.727530 \times 10^{-18}$	3.064270×10^{-9}	3.064270×10^{-9}

Table 3. Comparision of HAM and Numerical results for $f(\xi)$.

ξ	HAM	Numerical Solution	Absolute Error
0.0	1.000000	1.000000	0.000000
0.2	0.769682	0.769582	3.824810×10^{-7}
0.4	0.553068	0.553068	5.869700×10^{-8}
0.6	0.354231	0.354231	4.542170×10^{-7}
0.8	0.171895	0.171896	4.981640×10^{-7}
1.0	3.243540×10^{-17}	-1.553930×10^{-8}	1.553930×10^{-9}

Table 4. Comparision of HAM and Numerical results for $f(\xi)$.

ξ	HAM	Numerical Solution	Absolute Error
0.0	−1.030520	−1.015550	0.014980
0.2	−0.972080	−0.956321	0.015759
0.4	−1.001250	−0.982844	0.018401
0.6	−1.163130	−1.140120	0.023011
0.8	−1.495130	−1.465520	0.029607
1.0	−2.025290	−1.987240	0.038056

In Table 5, C_{fx} and C_{fy} are calculated for SWCNTs for a strong $K = 0$ (weak $K = 0.5$) concentration. It is observed that greater estimations of P_1 , E_r, and P_2 reduces C_{fx} and C_{fy} for both the $K = 0$ and $K = 0.5$ cases while the opposite effect is found for γ , N_r, and φ . In Table 6, C_{fx} and C_{fy} are calculated for MWCNTs for both $K = 0$ and $K = 0.5$. It is evident that higher estimations of P_1 , E_r, and P_2 increase C_{fx} and C_{fy} for both $K = 0$ and $K = 0.5$ while opposite results are found for γ , N_r, and φ .

Table 5. Variation in skin-friction coefficient C_{fx} and C_{fy} for single-walled carbon nanotubes (SWCNTs) together with strong and weak concentrations $K = 0$ and $K = 0.5$ and the comparison with previous results for fixed values of $Rd = 0.2$, $\delta = 0.1$, and $Re = 0.3$.

P_1	P_2	E_r	γ	N_r	φ	C_{fx} at $K = 0$ for SWCNT [56]	C_{fx} at $K = 0$ for SWCNT Present Values	C_{fy} at $K = 0.5$ for SWCNT [56]	C_{fy} at $K = 0.5$ for SWCNT Present Values
0.0	0.1	0.1	0.1	0.1	0.1	−1.47208	−1.93457	−1.47208	−1.14526
0.1						−1.58457	−1.72675	−1.52844	−1.19870
0.3						−2.03132	−1.99901	−1.75511	−1.24358
0.1	0.0					−1.58440	−1.64533	−1.52866	−1.99668
	0.3					−1.58453	−1.64337	−1.52849	−1.99650
	0.5					−1.58457	−1.64347	−1.52844	−1.99645
	0.1	0.1				−1.58265	−1.64555	−1.52558	−1.99660
		0.3				−1.59132	−1.64993	−1.53503	−2.10118
		0.5				−1.59977	−1.65001	−1.52849	−2.10110
		0.1	0.1			−1.58446	−1.64113	−1.53318	−2.10108
			0.3			−1.58477	−1.64783	−1.52848	−2.10318
			0.5			−1.58502	−1.65113	−1.52863	−2.10332
			0.1	0.1		−1.30696	−1.42001	−1.52863	−2.10337
				0.3		−1.02844	−1.34291	−1.52844	−2.10335
				0.5		−4.16259	−3.30023	−0.99212	−1.10002
				0.1	0.1	−2.95695	−3.14993	−4.01729	−3.80332
					0.3	−1.37247	−1.64793	−2.85298	−3.10300
					0.5	−1.44457	−1.64993	−1.32379	−1.23219
					0.1	−1.58457	−1.77903	−1.37935	−2.45332

Table 6. Variation in skin-friction coefficient C_{fx} and C_{fy} for multi-walled carbon nanotubes (MWCNTs) together with strong and weak concentrations $K = 0$ and $K = 0.5$ and the comparison with previous results for $Rd = 0.3$, $\delta = 0.1$, and $Re = 0.4$.

P_1	P_2	E_r	γ	N_r	φ	C_{fx} at K = 0 for MWCNT [56]	C_{fx} at K = 0 for MWCNT Present Values	C_{fy} at K = 0.5 for MWCNT [56]	C_{fy} at K = 0.5 for MWCNT Present Values
0.0	0.1	0.1	0.1	0.1	0.1	−1.61091	−1.93457	−1.61091	−1.83452
0.1						1.73404	−1.72321	−1.67259	−1.77433
0.3						−2.22304	−1.99881	−1.92069	−2.10032
0.1	0.0					−1.73386	−1.68751	−1.67283	−1.88643
	0.3					−1.73399	−1.68761	−1.67265	−1.88653
	0.5					−1.73404	−1.83450	−1.67259	−1.88647
	0.1	0.1				−1.73212	−1. 83324	−1.67070	−1.88601
		0.3				−1.74161	−1. 89022	−1.67989	−2.10111
		0.5				−1.75087	−1.74332	−1.68882	−1.88765
		0.1	0.1			−1.73403	−1. 83350	−1.67259	−2.00111
			0.3			−1.73422	−1. 83551	−1.67277	−1.98321
			0.5			−1.73476	−1. 83551	−1.67329	−1.98319
			0.1	0.1		−1.73404	−1. 83534	−1.67259	−1.10337
				0.3		−1.43009	−1. 53448	−1.37949	−2.10335
				0.5		−1.12523	−1.22910	−1.08546	−1.10002
				0.1	0.1	−4.55171	−3.99643	−4.39269	−3.80332
					0.3	−3.23473	−3.54643	−3.12094	−3.10300
					0.5	−1.50199	−1.32011	−1.44871	−1.23219
					0.1	−1.44457	−1.23199	−1.37935	−2.45332

In Table 7, the Nusselt number Nu_x for SWCNTs together with $K = 0$ and $K = 0.5$ are calculated. It is observed that higher estimations of P_1 increase Nu_x for $(K = 0)$ while it decreases Nu_x for $(K = 0.5)$, whereas increasing P_2 reduces Nu_x in the case of $(K = 0)$ and enhances it for $(K = 0.5)$. Furthermore, increasing values of J_1 , I_1, and Rd enhances Nu_x for $(K = 0)$ while it reduces Nu_x for $(K = 0.5)$. A higher value of φ reduces the heat flux. In Table 8, the Nusselt number Nu_x for MWCNTs together with $(K = 0)$ and $(K = 0.5)$ are calculated. Similar effects are observed as for that of Table 7 for MWCNTS in Table 8.

Table 7. Variation in the Nusselt numbers Nu_x for SWCNTs together with strong and weak concentrations $K = 0$ and $K = 0.5$ and the comparison with previous results for $E_r = 0.3$, $\delta = 0.2$, and $Re = 0.2$.

P_1	P_2	J_1	I_1	Rd	φ	Nu_x at K = 0 for SWCNT [56]	Nu_x at K = 0 for SWCNT Present Values	Nu_x at K = 0.5 for SWCNT [56]	C_{fy} at K = 0.5 for SWCNT Present Values
0.0	0.1	0.1	0.1	0.1	0.1	0.428266	0.938781	0.428266	0.938781
0.1						0.428328	0.938422	0.428259	0.938475
0.3						0.428217	0.938214	0.428230	0.938434
0.1	0.0					0.428278	0.937538	0.428261	0.937538
	0.3					0.428276	0.845373	0.428266	0.845473
	0.5					0.428274	0.845365	0.428259	0.845365
	0.1	0.1				.....	0.648742	.....	0.648546
		0.3				.....	0.649931	.....	0.649765
		0.5				.....	0.650013	.....	0.65563
		0.1	0.1			.....	0.641131	.....	0.641432
			0.3			.....	0.6478321	.....	0.647543
			0.5			.....	0.651131	.....	0.651665
			0.1	0.1		.....	0.420010	.....	0.423451
				0.3		.....	0.342914	.....	0.342914
				0.5		.....	0.300233	.....	0.300233
				0.1	0.1	0.433995	0.649936	0.433987	0.649936
					0.3	0.427375	0.642917	0.427370	0.642917
					0.5	0.425025	0.624327	0.425022	0.624327
					0.1	0.429519	0.779328	0.429512	0.779328

Table 8. Variation in Nu_x (the Nusselt numbers) for MWCNTs together with strong and weak concentrations $K = 0$ and $K = 0.5$ and the comparison with previous results for $E_r = 0.2$, $\delta = 0.1$, and $Re = 0.3$.

P_1	P_2	J_1	I_1	Rd	φ	Nu_x at K = 0 for MWCNT [56]	Nu_x at K = 0 for MWCNT Present Values	Nu_x at K = 0.5 for MWCNT [56]	C_{fy} at K = 0.5 for MWCNT Present Values
0.0	0.1	0.1	0.1	0.1	0.1	0.429005	0.93457	0.429005	0.93878
0.1						0.429069	0.93675	0.428998	0.99883
0.3						0.429061	0.93901	0.428966	0.99958
0.1	0.0					0.429019	0.93533	0.428996	0.99968
	0.3					0.429015	0.93337	0.429005	0.99650
	0.5					0.429013	0.93347	0.429008	0.99045
	0.1	0.1				.....	0.94557	.....	0.99660
		0.3				.....	0.94990	.....	0.90118
		0.5				.....	0.95032	.....	0.90110
		0.1	0.1			.....	0.94533	.....	0.90108
			0.3			.....	0.94783	.....	0.90318
			0.5			.....	0.95113	.....	0.90332
			0.1	0.1		.....	0.92021	.....	0.90337
				0.3		.....	0.94291	.....	0.90333
				0.5		.....	0.95023	.....	0.90002
				0.1	0.1	0.430229	0.94993	0.430221	0.80332
					0.3	0.429013	0.94793	0.429007	0.80300
					0.5	0.427787	0.94993	0.427783	0.83219

The effect of P_r (Prandtl number) on Nu_x (Nusselt number) in the case of $\varphi = 0$ (regular fluid) is displayed in Table 9. We see that the present results agree with the published results of Shah et al. [43, 56]. In Table 10, some precarious physical characteristics of the CNTs are tabulated. Table 11 displays the impact of φ on the thermal conductivity k_{nf}. It is apparent that, for CNTs, the thermal conductivity changes with the increasing φ.

Table 9. Influence of Prandtl number Pr on Nusselt number Nu at $\varphi = 0$.

Pr	Nu [56] Results	Nu [43] Results	Nu Present Results
0.71	0.47	0.477	0.488
7.0	1.491	1.522	1.989
0.71	0.33	0.345	0.547

Table 10. Several physical characteristics of CNTs and different nanofluids.

Base fluids	Nanofluids	$c_p\left(\frac{K^{-1}}{Kg}\right)$	$\rho\left(\frac{Kg}{m^3}\right)$	$k\left(\frac{W}{mK}\right)$
Water		41.97×10^2	0.997×10^3	6.13×10^{-1}
Kerosene (lamp oil)		20.90×10^2	7.83×10^{22}	1.45×10^{-1}
Engine oil		19.10×10^2	8.84×10^2	1.44×10^{-1}
	SWCNT	0.425×10^3	2.6×10^3	6.6×10^3
	MWCNT	0.796×10^3	1.6×10^3	3×10^3

Table 11. Influence of the volume fraction φ on thermal conductivity k_{nf}.

φ	k_{nf} for SWCNT	k_{nf} for MWCNT
0	14.5×10^{-2}	14.5×10^{-2}
0.01	17.4×10^{-2}	17.2×10^{-2}
0.02	20.4×10^{-2}	0.2×10^{-2}
0.03	23.5×10^{-2}	22.8×10^{-2}
0.04	26.6×10^{-2}	25.5×10^{-2}

5. Conclusions

The three-dimensional flow of Darcy–Forchheimer micro-polar nanofluid water-based carbon nanotubes in a rotatory frame has been examined in this research work. The impacts of rotation parameter, permeability parameter, coefficient of inertia, coupling parameter, viscosity gradient parameter, Reynold number, and thermal

radiation are emphasized in this work. The fluid flow is studied under the assumptions of weak and strong concentrations. The key points are given as below:

- The upsurge in Re, N_r , P_1 , φ , and E_r show dual behavior in the profile of $f^{'}(\xi)$.
- The upsurge in E_r exhibits dual behavior in the $g(\xi)$ profile.
- The higher φ, γ, and Re values escalate $g(\xi)$.
- The higher N_r and P_1 values decline the $g(\xi)$ profile .
- The larger φ, P_1, and Re values cause an increase in $G(\xi)$.
- The higher φ, Rd , J_1, and I_1 values result in a rise in the $\theta(\xi)$ profile.
- The upsurges in P_1 , E_r, and γ reduce C_f for SWCNTs along the x and y-directions for both strong and weak concentrations, while it increases with the escalation in N_r .
- The higher values of P_1 , J_1 , I_1, and Rd increase the Nusselt number Nu_x for strong concentrations while reduces it for weak concentrations for both SWCNTs and MWCNTs.

Author Contributions: Conceptualization, E.O.A. and Z.S.; methodology, W.A.; software, Z.S.; validation, E.O.A., Z.S., and M.Z.U.; formal analysis, E.O.A.; investigation, Z.S.; resources, M.Z.U.; data curation, W.A.; writing–original draft preparation, M.Z.U.; writing–review and editing, E.O.A.; visualization, Z.S.; supervision, E.O.A.

Acknowledgments: This project was funded by the Deanship of Scientific Research (DSR) at King Abdulaziz University, Jeddah under grant no. (RG-85-130-38). The authors, therefore, gratefully acknowledge DSR for technical and financial support.

Conflicts of Interest: The authors declare no conflict of interest.

References

1. Iijima, S. Helical microtubules of graphitic carbon. *Nature* **1991**, *354*, 56. [CrossRef]
2. Ciraci, S.; Dag, S.; Yildirim, T.; Gülseren, O.; Senger, R. Functionalized carbon nanotubes and device applications. *J. Phys. Condens. Matter.* **2004**, *16*, R901. [CrossRef]
3. Novoselov, K.S.; Geim, A.K.; Morozov, S.V.; Jiang, D.; Zhang, Y.; Dubonos, S.V.; Grigorieva, I.V.; Firsov, A.A. Electric field effect in atomically thin carbon films. *Science* **2004**, *306*, 666–669. [CrossRef] [PubMed]
4. Casari, C.S.; Tommasini, M.; Tykwinski, R.R.; Milani, A. Carbon-atom wires: 1-D systems with tunable properties. *Nanoscale* **2016**, *8*, 4414–4435. [CrossRef] [PubMed]
5. Ellahi, R.; Zeeshan, A.; Hussain, F.; Abbas, T. Two-Phase Couette Flow of Couple Stress Fluid with Temperature Dependent Viscosity Thermally Affected by Magnetized Moving Surface. *Symmetry* **2019**, *11*, 647. [CrossRef]
6. Marin, M.; Vlase, S.; Ellahi, R.; Bhatti, M. On the Partition of Energies for the Backward in Time Problem of Thermoelastic Materials with a Dipolar Structure. *Symmetry* **2019**, *11*, 863. [CrossRef]
7. Prakash, J.; Tripathi, D.; Triwari, A.; Sait, S.M.; Ellahi, R. Peristaltic Pumping of Nanofluids through a Tapered Channel in a Porous Environment: Applications in Blood Flow. *Symmetry* **2019**, *11*, 868. [CrossRef]
8. Imtiaz, M.; Hayat, T.; Alsaedi, A.; Ahmad, B. Convective flow of carbon nanotubes between rotating stretchable disks with thermal radiation effects. *Int. J. Heat Mass Transf.* **2016**, *101*, 948–957. [CrossRef]
9. Hayat, T.; Haider, F.; Muhammad, T.; Alsaedi, A. On Darcy-Forchheimer flow of carbon nanotubes due to a rotating disk. *Int. J. Heat Mass Transf.* **2017**, *112*, 248–254. [CrossRef]
10. Mahanthesh, B.; Gireesha, B.; Shashikumar, N.; Shehzad, S. Marangoni convective MHD flow of SWCNT and MWCNT nanoliquids due to a disk with solar radiation and irregular heat source. *Phys. E Low-Dimens. Syst. Nanostruct.* **2017**, *94*, 25–30. [CrossRef]
11. Raja, M.A.Z.; Ahmed, T.; Shah, S.M. Intelligent computing strategy to analyze the dynamics of convective heat transfer in MHD slip flow over stretching surface involving carbon nanotubes. *J. Taiwan Inst. Chem. Eng.* **2017**, *80*, 935–953. [CrossRef]
12. Shah, Z.; Dawar, A.; Islam, S.; Khan, I.; Ching, D.L.C. Darcy-Forchheimer flow of radiative carbon nanotubes with microstructure and inertial characteristics in the rotating frame. *Case Stud. Therm. Eng.* **2018**, *12*, 823–832. [CrossRef]
13. Jawad, M.; Shah, Z.; Islam, S.; Majdoubi, J.; Tlili, I.; Khan, W.; Khan, I. Impact of nonlinear thermal radiation and the viscous dissipation effect on the unsteady three-dimensional rotating flow of single-wall carbon nanotubes with aqueous suspensions. *Symmetry* **2019**, *11*, 207. [CrossRef]

14. Kandelousi, M.S. KKL correlation for simulation of nanofluid flow and heat transfer in a permeable channel. *Phys. Lett. A* **2014**, *378*, 3331–3339. [CrossRef]
15. Sheikholeslami, M. Numerical simulation of magnetic nanofluid natural convection in porous media. *Phys. Lett. A* **2017**, *381*, 494–503. [CrossRef]
16. Sheikholeslami, M.; Shamlooei, M. Magnetic source influence on nanofluid flow in porous medium considering shape factor effect. *Phys. Lett. A* **2017**, *381*, 3071–3078. [CrossRef]
17. Shah, Z.; Gul, T.; Islam, S.; Khan, M.A.; Bonyah, E.; Hussain, F.; Mukhtar, S.; Ullah, M. Three dimensional third grade nanofluid flow in a rotating system between parallel plates with Brownian motion and thermophoresis effects. *Results Phys.* **2018**, *10*, 36–45. [CrossRef]
18. Shah, Z.; Islam, S.; Ayaz, H.; Khan, S. Radiative heat and mass transfer analysis of micropolar nanofluid flow of Casson fluid between two rotating parallel plates with effects of Hall current. *J. Heat Transf.* **2019**, *141*, 022401. [CrossRef]
19. Shah, Z.; Islam, S.; Gul, T.; Bonyah, E.; Khan, M.A. The electrical MHD and hall current impact on micropolar nanofluid flow between rotating parallel plates. *Results Phys.* **2018**, *9*, 1201–1214. [CrossRef]
20. Dawar, A.; Shah, Z.; Idrees, M.; Khan, W.; Islam, S.; Gul, T. Impact of thermal radiation and heat source/sink on Eyring–Powell fluid flow over an unsteady oscillatory porous stretching surface. *Math. Comput. Appl.* **2018**, *23*, 20. [CrossRef]
21. Ullah, A.; Alzahrani, E.; Shah, Z.; Ayaz, M.; Islam, S. Nanofluids thin film flow of Reiner-Philippoff fluid over an unstable stretching surface with Brownian motion and thermophoresis effects. *Coatings* **2019**, *9*, 21. [CrossRef]
22. Ameen, I.; Shah, Z.; Islam, S.; Nasir, S.; Khan, W.; Kumam, P.; Thounthong, P. Hall and Ion-Slip Effect on CNTS Nanofluid over a Porous Extending Surface through Heat Generation and Absorption. *Entropy* **2019**, *21*, 801. [CrossRef]
23. Dawar, A.; Shah, Z.; Islam, S.; Idress, M.; Khan, W. Magnetohydrodynamic CNTs Casson Nanofl uid and Radiative heat transfer in a Rotating Channels. *J. Phys. Res. Appl.* **2018**, *1*, 017–032.
24. Sohail, A.; Fatima, M.; Ellahi, R.; Akram, K.B. A videographic assessment of Ferrofluid during magnetic drug targeting: An application of artificial intelligence in nanomedicine. *J. Mol. Liq.* **2019**, *285*, 47–57. [CrossRef]
25. Zeeshan, A.; Majeed, A.; Ellahi, R. Effect of magnetic dipole on viscous ferro-fluid past a stretching surface with thermal radiation. *J. Mol. Liq.* **2016**, *215*, 549–554. [CrossRef]
26. Majeed, A.; Zeeshan, A.; Ellahi, R. Unsteady ferromagnetic liquid flow and heat transfer analysis over a stretching sheet with the effect of dipole and prescribed heat flux. *J. Mol. Liq.* **2016**, *223*, 528–533. [CrossRef]
27. Eringen, A.C. Theory of micropolar fluids. *J. Math. Mech.* **1966**, *16*, 1–18. [CrossRef]
28. Lukaszewicz, G. *Micropolar Fluids: Theory and Applications*; Springer: Berlin/Heidelberg, Germany, 1999.
29. Mohammadein, A.; Gorla, R. Effects of transverse magnetic field on mixed convection in a micropolar fluid on a horizontal plate with vectored mass transfer. *Acta Mech.* **1996**, *118*, 1–12. [CrossRef]
30. Khan, A.; Shah, Z.; Islam, S.; Khan, S.; Khan, W.; Khan, A.Z. Darcy–Forchheimer flow of micropolar nanofluid between two plates in the rotating frame with non-uniform heat generation/absorption. *Adv. Mech. Eng.* **2018**, *10*. [CrossRef]
31. Forchheimer, P. Wasserbewegung durch Boden. *Z. Ver. German Ing.* **1901**, *45*, 1782–1788.
32. Muskat, M. *The Flow of Homogeneous Fluids through Porous Media*; J.W. Edwards, Inc.: Ann Arbor, MI, USA, 1946.
33. Cheng, P.; Minkowycz, W. Free convection about a vertical flat plate embedded in a porous medium with application to heat transfer from a dike. *J. Geophys. Res.* **1977**, *82*, 2040–2044. [CrossRef]
34. Merkin, J. Free convection boundary layers on axi-symmetric and two-dimensional bodies of arbitrary shape in a saturated porous medium. *Int. J. Heat Mass Transf.* **1979**, *22*, 1461–1462. [CrossRef]
35. Nakayama, A.; Koyama, H. Free convective heat transfer over a nonisothermal body of arbitrary shape embedded in a fluid-saturated porous medium. *J. Heat Transf.* **1987**, *109*, 125–130. [CrossRef]
36. Jawad, M.; Shah, Z.; Islam, S.; Bonyah, E.; Khan, A.Z. Darcy-Forchheimer flow of MHD nanofluid thin film flow with Joule dissipation and Navier's partial slip. *J. Phys. Commun.* **2018**, *2*, 115014. [CrossRef]
37. Khan, N.S.; Zuhra, S.; Shah, Z.; Bonyah, E.; Khan, W.; Islam, S. Slip flow of Eyring-Powell nanoliquid film containing graphene nanoparticles. *AIP Adv.* **2018**, *8*, 115302. [CrossRef]

38. Khan, A.; Nie, Y.; Shah, Z.; Dawar, A.; Khan, W.; Islam, S. Three-dimensional nanofluid flow with heat and mass transfer analysis over a linear stretching surface with convective boundary conditions. *Appl. Sci.* **2018**, *8*, 2244. [CrossRef]
39. Nasir, S.; Islam, S.; Gul, T.; Shah, Z.; Khan, M.A.; Khan, W.; Khan, A.Z.; Khan, S. Three-dimensional rotating flow of MHD single wall carbon nanotubes over a stretching sheet in presence of thermal radiation. *Appl. Nanosci.* **2018**, *8*, 1361–1378. [CrossRef]
40. Dawar, A.; Shah, Z.; Kumam, P.; Khan, W.; Islam, S. Influence of MHD on Thermal Behavior of Darcy-Forchheimer Nanofluid Thin Film Flow over a Nonlinear Stretching Disc. *Coatings* **2019**, *9*, 446. [CrossRef]
41. Ellahi, R.; Sait, S.M.; Shehzad, N.; Mobin, N. Numerical Simulation and Mathematical Modeling of Electro-Osmotic Couette–Poiseuille Flow of MHD Power-Law Nanofluid with Entropy Generation. *Symmetry* **2019**, *11*, 1038. [CrossRef]
42. Raju, C.; Sandeep, N.; Malvandi, A. Free convective heat and mass transfer of MHD non-Newtonian nanofluids over a cone in the presence of non-uniform heat source/sink. *J. Mol. Liq.* **2016**, *221*, 108–115. [CrossRef]
43. Sheikholeslami, M.; Shah, Z.; Shafee, A.; Khan, I.; Tlili, I. Uniform magnetic force impact on water based nanofluid thermal behavior in a porous enclosure with ellipse shaped obstacle. *Sci. Rep.* **2019**, *9*, 1196. [CrossRef] [PubMed]
44. Rehman, F.; Khan, M.I.; Sadiq, M.; Malook, A. MHD flow of carbon in micropolar nanofluid with convective heat transfer in the rotating frame. *J. Mol. Liq.* **2017**, *231*, 353–363. [CrossRef]
45. Hayat, T.; Sajjad, R.; Muhammad, T.; Alsaedi, A.; Ellahi, R. On MHD nonlinear stretching flow of Powell–Eyring nanomaterial. *Results Phys.* **2017**, *7*, 535–543. [CrossRef]
46. Tian, X.Y.; Li, B.W.; Hu, Z.M. Convective stagnation point flow of a MHD non-Newtonian nanofluid towards a stretching plate. *Int. J. Heat Mass Transf.* **2018**, *127*, 768–780. [CrossRef]
47. Hsiao, K.L. Combined electrical MHD heat transfer thermal extrusion system using Maxwell fluid with radiative and viscous dissipation effects. *Appl. Therm. Eng.* **2017**, *112*, 1281–1288. [CrossRef]
48. Hsiao, K.L. Micropolar nanofluid flow with MHD and viscous dissipation effects towards a stretching sheet with multimedia feature. *Int. J. Heat Mass Transf.* **2017**, *112*, 983–990. [CrossRef]
49. Feroz, N.; Shah, Z.; Islam, S.; Alzahrani, E.O.; Khan, W. Entropy generation of carbon nanotubes flow in a rotating channel with hall and ion-slip effect using effective thermal conductivity model. *Entropy* **2019**, *21*, 52. [CrossRef]
50. Ellahi, R.; Raza, M.; Akbar, N.S. Study of peristaltic flow of nanofluid with entropy generation in a porous medium. *J. Porous Media* **2017**, *20*, 461–478. [CrossRef]
51. Esfahani, J.A.; Akbarzadeh, M.; Rashidi, S.; Rosen, M.; Ellahi, R. Influences of wavy wall and nanoparticles on entropy generation over heat exchanger plat. *Int. J. Heat Mass Transf.* **2017**, *109*, 1162–1171. [CrossRef]
52. Ellahi, R.; Zeeshan, A.; Hussain, F.; Asadollahi, A. Peristaltic blood flow of couple stress fluid suspended with nanoparticles under the influence of chemical reaction and activation energy. *Symmetry* **2019**, *11*, 276. [CrossRef]
53. Khan, N.S.; Shah, Z.; Islam, S.; Khan, I.; Alkanhal, T.A.; Tlili, I. Entropy generation in MHD mixed convection non-Newtonian second-grade nanoliquid thin film flow through a porous medium with chemical reaction and stratification. *Entropy* **2019**, *21*, 139. [CrossRef]
54. Khan, A.S.; Nie, Y.; Shah, Z. Impact of thermal radiation and heat source/sink on MHD time-dependent thin-film flow of Oldroyed-B, Maxwell, and Jeffry Fluids over a stretching surface. *Processes* **2019**, *7*, 191. [CrossRef]
55. Nasir, S.; Shah, Z.; Islam, S.; Bonyah, E.; Gul, T. Darcy Forchheimer nanofluid thin film flow of SWCNTs and heat transfer analysis over an unsteady stretching sheet. *AIP Adv.* **2019**, *9*, 015223. [CrossRef]
56. Shah, Z.; Bonyah, E.; Islam, S.; Gul, T. Impact of thermal radiation on electrical mhd rotating flow of carbon nanotubes over a stretching sheet. *AIP Adv.* **2019**, *9*, 015115. [CrossRef]
57. Ali, A.; Sulaiman, M.; Islam, S.; Shah, Z.; Bonyah, E. Three-dimensional magnetohydrodynamic (MHD) flow of Maxwell nanofluid containing gyrotactic micro-organisms with heat source/sink. *AIP Adv.* **2018**, *8*, 085303. [CrossRef]
58. Shah, Z.; Bonyah, E.; Islam, S.; Khan, W.; Ishaq, M. Radiative MHD thin film flow of Williamson fluid over an unsteady permeable stretching sheet. *Heliyon* **2018**, *4*, e00825. [CrossRef] [PubMed]

59. Ullah, A.; Shah, Z.; Kumam, P.; Ayaz, M.; Islam, S.; Jameel, M. Viscoelastic MHD Nanofluid Thin Film Flow over an Unsteady Vertical Stretching Sheet with Entropy Generation. *Processes* **2019**, *7*, 262. [CrossRef]
60. Shah, Z.; Ullah, A.; Bonyah, E.; Ayaz, M.; Islam, S.; Khan, I. Hall effect on Titania nanofluids thin film flow and radiative thermal behavior with different base fluids on an inclined rotating surface. *AIP Adv.* **2019**, *9*, 055113. [CrossRef]
61. Xue, Q. Model for thermal conductivity of carbon nanotube-based composites. *Phys. B Condens. Matter* **2005**, *368*, 302–307. [CrossRef]